Chapter 2

Growth of Germanium, Silicon, and Ge–Si Heterostructured Nanowires

Shadi A. Dayeh and S. Thomas Picraux
Center for Integrated Nanotechnologies, Los Alamos National Laboratory, Los Alamos, NM 87545, USA
picraux@lanl.gov

2.1 Introduction

Anisotropic growth of one-dimensional (1-D) crystals has been the subject of research from as early as the 1950s.[1,2] Such studies intensified with the discovery of the vapor–liquid–solid (VLS) mechanism for silicon wires in 1964[3] and gained global interest in nanoscale science and engineering since the 1990s.[4,5] The 1-D structure of nanometer scale wires, or nanowires(NWs), serves as a platform for understanding basic materials science[6] and surface science behavior[7] as well as electron,[8] photon,[9] phonon,[10] and ion[11] transport phenomena at reduced dimensions. Numerous applications in electronics,[12] photonics,[13] thermoelectrics,[14] and energy storage[15] have been postulated and are being pursued. To achieve full control over the properties of NW structures, uncover

Silicon and Silicide Nanowires: Applications, Fabrication, and Properties
Edited by Yu Huang and King-Ning Tu
Copyright © 2014 Pan Stanford Publishing Pte. Ltd.
ISBN 978-981-4303-46-0 (Hardcover), 978-981-4303-47-7 (eBook)
www.panstanford.com

© 2013 by Taylor & Francis Group, LLC

the underlying mechanisms that control such properties, and exploit their promise for technological applications, a greater understanding of growth mechanisms, structure, and properties is needed. Even further opportunities to achieve new properties may be anticipated by combining different materials into heterostructured NWs.

Since the general features of semiconductor NW synthesis and growth mechanisms have been discussed in review articles in the literature,[12,13,16,17] we concentrate in this chapter on the specific aspects of size effects in Ge and Si NW growth, defect formation during growth, and the understanding of growth mechanisms to synthesize heterostructured Si and Ge combinations in axial and radial directions. We have two main goals in this chapter. The first goal is to provide new perspective on the VLS mechanism and concrete experimental evidence on size effects in semiconductor NW synthesis, as well as to resolve relevant controversies about this effect. The second is to discuss the VLS growth of heterostructures with examples of the growth mechanisms and challenges, and the resultant NW morphologies. For background we first provide an overview of the VLS mechanism and its application to Ge and Si NWs. We then discuss the effects of small size on VLS growth and introduce the critical radius for suppression of the VLS growth mechanism. The underlying thermodynamic mechanism giving rise to these effects is illustrated through the influence of temperature, pressure, and surface energies on VLS growth at small size. We then discuss semiconductor NW heterostructure growth, beginning with ledge nucleation and fault propagation during VLS growth and followed by a broader discussion of Ge–Si axial and radial heterostructure growth. The novel aspects of such heterostructures are highlighted by an example of an energy band-edge-engineered device that is uniquely achieved by VLS heterostructure growth.

2.2 The VLS Growth Mechanism

Growth of metal-catalyzed semiconductor NWs using chemical vapor deposition techniques is generally accepted to follow the VLS growth mechanism[3] which uses a metallic nanoparticle, typically Au, that forms a low-temperature liquid eutectic with the desired growth material (Fig. 2.1a). Gas precursors containing reactant material are introduced and catalytically decompose with the incorporation of

Downloaded by [University of California - San Diego (CDL)] at 19:53 11 December 2013

© 2013 by Taylor & Francis Group, LLC

the growth species through the nanoparticle surface forming a liquid droplet near the eutectic temperature. This liquid droplet continues to adsorb decomposing solute atoms from the vapor, leading to a supersaturated state (Fig. 2.1b), at which point crystallization of the semiconductor occurs at the liquid–solid interface resulting in 1-D NW growth (Fig. 2.1c).

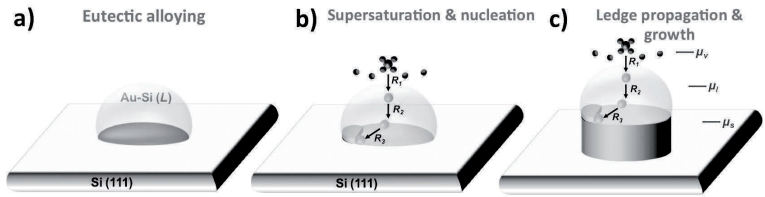

Figure 2.1 Schematic illustration of the VLS process for Si NWs. (a) A heated Si (111) substrate with a Au nanoparticle atop forms an eutectic molten nanoparticle. (b) Introduction of gas precursors (SiH_4 or $SiCl_4$) decompose at the particle surface and Si atoms diffuse into the nanoparticle which reaches a supersaturated state leading to the onset of ledge nucleation. (c) Continuation of ledge nucleation and propagation at the liquid–solid interface leads the growth of a Si NW with a diameter set by the starting Au nanoparticle diameter.

The most fascinating and distinguishing aspects of the VLS process arise from the use of the liquid metal–semiconductor alloy catalyst. Some of these remarkable aspects include (i) growth of semiconductor crystals at temperatures much lower than those used in thin film growth,[18] (ii) high diffusivity of reactant materials through or at the surface of the eutectic particle,[19] and (iii) the formation of a single nucleus, typically at the triple-phase (VLS) boundary,[20] followed by (iv) rapid ledge propagation during atomic layer growth.[21] These particular aspects are what lead to the relatively high NW-growth rates mediated by the eutectic particle, and the formation of crystals with well-predicted crystallographic structure.

In the case of growth of the isoelectronic Ge–Si materials system, a number of basic thermodynamic and kinetic considerations take effect. The metal nanoparticle—semiconductor system Au–Ge or Au–Si must reach a liquid condition prior to ledge formation in VLS NW growth. Considering the bulk phase diagram shown in

Downloaded by [University of California - San Diego (CDL)] at 19:53 11 December 2013

© 2013 by Taylor & Francis Group, LLC

Downloaded by [University of California - San Diego (CDL)] at 19:53 11 December 2013

Fig. 2.2a, the eutectic temperature for Au–Ge and Au–Si is ~360 °C. In nanoscale alloys, we show below that the eutectic temperature can be significantly lower than in bulk materials. Moreover, *in situ* electron microscopy studies of nucleation of a liquid phase for a Au–Ge nanoparticle system has been shown to occur at much lower temperatures than in the bulk Au–Ge system.[22] We denote in Fig. 2.2a an approximate temperature and composition range over which growth of Ge and Si NWs can occur.[18] The precise temperatures for growth experiments are inevitably pressure dependent since the decomposition efficiency of the widely used precursors GeH_4 and SiH_4 for Ge and Si NW growth, respectively, is pressure dependent. GeH_4 is fully decomposed at a temperature of 280 °C,[23] and SiH_4 at a temperature of ~600 °C.[24] This therefore dictates that growth of Si NWs is generally accomplished at temperatures higher than the eutectic temperature of 360 °C as shown in Fig. 2.2a whereas Ge NW growth extends to temperatures below the eutectic point.

Aside from the eutectic formation, the Au–Ge or Au–Si system must reach a supersaturated state with a difference in the chemical potentials (Fig. 2.1c) expressed as

$$\Delta\mu = \mu_v - \mu_s \cong \mu_l - \mu_s = kT\ln(P_{in} / P_{0(NW)}), \tag{2.1}$$

where μ_v, μ_l, and μ_s are the chemical potentials of Ge or Si in the vapor, liquid, and solid phases respectively, k is Boltzmann's constant, T is the temperature in K, P_{in} is the input partial pressure of Ge or Si adatoms, $P_{0(NW)}$ is the equilibrium partial pressure of Ge or Si in Au. $P_{0(NW)}$ can be expressed as[25]

$$P_{0(NW)} = P_\infty \left(e^{\frac{4\Omega\alpha_{vl}}{dkT}} \right) \cong P_\infty \left(e^{\frac{4\Omega\alpha_{vs}}{dkT}} \right), \tag{2.2}$$

where P_∞ is the partial pressure of Ge or Si in infinite Au medium, Ω is the atomic volume of liquid Ge or Si in Au, α_{vl} is the surface energy density of the eutectic particle, α_{vs} is the surface energy density of Ge or Si sidewall facets under typical NW growth temperatures, and d is the NW diameter. Under typical growth conditions, say for Ge, $\alpha_{vl} \approx \alpha_{vs}$ ($\alpha_{vl} \sim 0.78$ J/m^2 and 0.8 J/m^2 for temperatures of 404 °C and 470 °C, respectively, which is similar to the (110) Ge surface energy density of 0.88 J/m^2).[26] This difference in α_{vl}, α_{vs} is typically neglected in the literature.[27] Using Henrys law ($P_i = k_H C_i$), where k_H is a constant, together with Eqs. 2.1 and 2.2, we can express the

© 2013 by Taylor & Francis Group, LLC

Downloaded by [University of California - San Diego (CDL)] at 19:53 11 December 2013

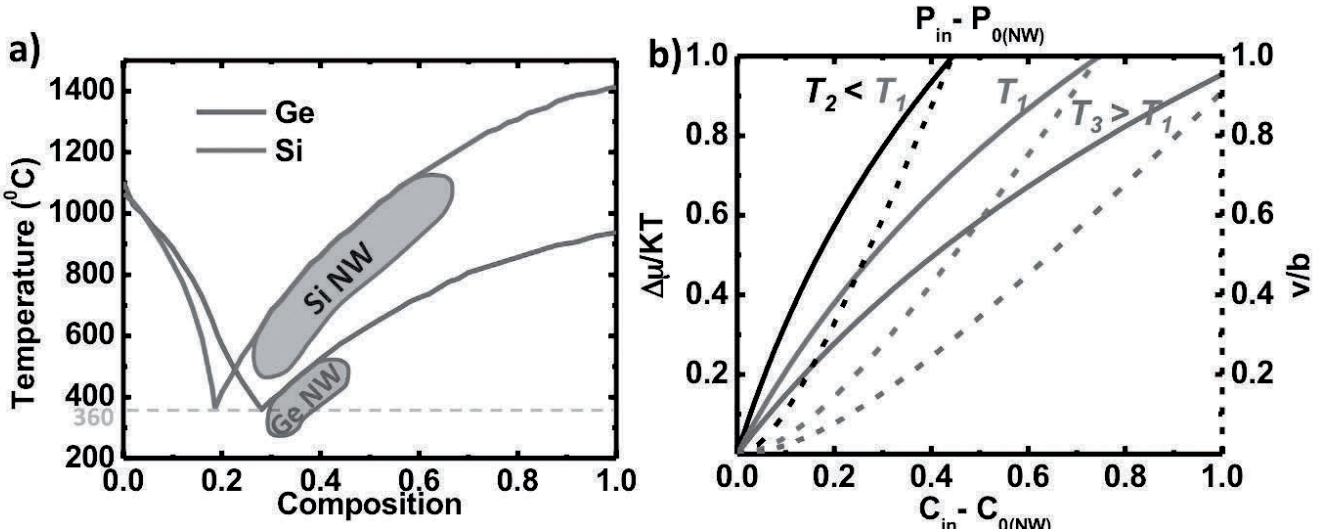

Figure 2.2 (a) Bulk phase diagrams of Ge and Si with highlighted regions of Ge and Si NW growth under commonly used CVD growth conditions. (b) Plot of the normalized supersaturation, $\Delta\mu/kT$, and the normalized growth rate, v/b, as a function of the input concentration gradient, C_{in}–$C_{0(NW)}$, or partial pressure gradient, P_{in}–$P_{0(NW)}$, of input precursors at the vapor–liquid interface to those in the liquid eutectic at equilibrium [liquidus line in (a)].

© 2013 by Taylor & Francis Group, LLC

concentration gradient of Ge between the surface of the eutectic alloy (vapor–liquid), C_{in}, and the equilibrium concentration of Ge at the NW growth surface (liquid–solid) at, $C_{0(NW)}$, as

$$C_{in} - C_{0(NW)} = C_{\infty}\left(e^{\frac{4\Omega\alpha_{vs}}{dkT}}\right)\left(e^{\frac{\Delta\mu}{kT}} - 1\right). \quad (2.3)$$

Equation 2.3 portrays the important influence of thermodynamic and kinetic effects on NW growth behavior, and is plotted in Fig. 2.2b. For a constant diameter and at a constant temperature T_1 an increase in the input precursor partial pressure (equivalent to an increase in input concentration gradient) leads to an increase in the effective supersaturation, $\Delta\mu/kT$, and therefore an increase in the growth rate. In Fig. 2.2b, the normalized growth velocity, v/b, is plotted to exclude additional kinetic effects such as precursor decomposition or reaction rate at the liquid–solid interface, as will be discussed in the temperature section. As the temperature decreases toward the eutectic temperature (i.e., moving left on the liquidus line), the equilibrium concentration of Ge or Si in Au decreases as shown in Fig. 2.2a. Therefore, for the same input partial pressure, the supersaturation and consequently the normalized growth rate must increase as the temperature is increased as depicted for the case of $T_2 < T_1$ in Fig. 2.2b. On the other hand, as the temperature is increased further away from the eutectic point (i.e., moving right on the liquidus line), the equilibrium concentration of Ge or Si in Au increases and the supersaturation and consequently the normalized growth rate must decrease as shown for the case of $T_3 > T_1$ in Fig. 2.2b. This unified picture of the VLS growth precisely depicts our experimental observations on the dependence of Ge NW growth rate on temperature and pressure, as discussed in the forthcoming sections.

To expand further on the VLS framework introduced above, we put the analysis in the context of the three processes commonly debated as rate-limiting steps in the VLS growth. These processes, depicted in Fig. 2.1c, include (1) incorporation rate at the vapor–liquid interface by precursor decomposition, R_1, (2) diffusion rate through the Au particle, R_2, and (3) crystallization rate at the liquid–solid interface, R_3, limited by nucleation of step ledges.[28] R_2 is not limiting but resembles a unique aspect of the VLS growth compared with the vapor–solid–solid (VSS) growth. It is the fast reactant (Ge or Si) diffusion in the liquid growth seed that enables fast growth rates

Downloaded by [University of California - San Diego (CDL)] at 19:53 11 December 2013

© 2013 by Taylor & Francis Group, LLC

with excellent morphological control and high aspect ratios in VLS grown NWs compared with VSS grown NWs whose axial elongation rate is not fast enough compared with its sidewall deposition growth rate for comparable high aspect ratio NW growth.[28,29]

Considering the case of Ge NW growth, R_1 resembles an equilibrium reaction of GeH_4 decomposition at the vapor–liquid interface and R_3 resembles a nucleation reaction at the liquid–solid interface. In steady state, these two rates are equal such that the amount of Ge consumed by R_3 at the liquid–solid interface is equal to the amount of Ge supplied by R_1 from the vapor–liquid interface (both are area normalized), and the growth proceeds at the liquid–solid interface according to a chemical potential difference $\Delta\mu_{vs}$ expressed in Eq. 2.1. If the NW diameter decreases, at otherwise constant temperature and pressure, μ_s increases and $\Delta\mu_{vs}$ decreases (see Eq. 2.4) leading to lower growth rates. In this case, R_3 decreases and consequently, R_1 decreases by a reduction of the rate constant of GeH_4 decomposition and incorporation at the vapor–liquid interface. For a constant diameter and temperature, if the GeH_4 partial pressure increases, R_1 increases and consequently R_3 increases leading to a higher growth rate, as we will discuss in the *Pressure Effects* section. From this, we conclude that during steady state NW growth, it is misleading to isolate either R_1 or R_3 as the rate-limiting step, as these are by definition equal during steady state growth. For a constant diameter and pressure, if the temperature increases, $\Delta\mu_{vs}$ decreases but the temperature-dependent reaction constants at the vapor–liquid interface increases R_1 and similarly at the liquid–solid interface increases R_3 leading to higher growth rates with temperature.

Since elemental group IV NWs typically utilize a single growth precursor, validation of the VLS concepts discussed above eliminates complexities and misinterpretations which can arise in the growth of other compound semiconductor NWs. The concepts themselves however are generally applicable to any material system undergoing the VLS growth mechanism provided all rate-limiting factors are taken into account. For example, in the binary III–V compounds, differences of decomposition temperatures[30] and the different adatom mean free paths[31] need to be accounted for. In almost every NW materials system, a kinetically limited growth behavior, that is, increase in growth velocity with temperature, is observed.[32,33] For the special case of III–V semiconductor NWs, the solubility of

Downloaded by [University of California - San Diego (CDL)] at 19:53 11 December 2013

© 2013 by Taylor & Francis Group, LLC

group III materials is generally orders of magnitude higher than that of the group V species.[34] The eutectic growth nanoparticle comprises therefore of Au-group III composition. Since the mean free path of group III is dependent on temperature and the relative molar fraction of group V to group III, diffusion of group III to the nanoparticle can be limited by the complex interplay between these two growth precursors.[31] As such, a high growth temperature can increase the amount of decomposed group V precursor and reduce the surface mobility of In to the Au or Au–In nanoparticle leading to suppression or complete cessation of III–V NW growth at higher temperatures.[30] We state therefore that pulling the growth conditions largely away from those that produce uniform NW morphologies, for any semiconductor NW material system, can lead to significant deviation from the growth model discussed above and consequent misinterpretation of experimental data. Care must be exercised when applying the VLS concept to any materials system that is more complex than the monatomic Ge or Si systems, as well as under the presence of contaminants or low pressures and/or temperatures, including for Ge and Si NW materials growth.

2.3 Size Effects in Nanowire Growth

The diameter and consequently the electronic and optical properties of NWs are dependent on the size of the metal nanoparticle. Substituting Eq. 2.1 into Eq. 2.2, we get

$$\frac{\Delta\mu}{kT} = \frac{\Delta\mu_0}{kT} - \frac{1}{kT}\frac{4\alpha_{vs}}{d}. \tag{2.4}$$

where $\Delta\mu_0$ is the supersaturation of the semiconductor material for an infinite medium (i.e., the bulk limit of a planar surface for the catalytic growth particle). Equation 2.4 has a number of consequences for size-dependent semiconductor NW growth. First, as the diameter of the NW decreases the magnitude of the right hand term increases, and this corresponds to a reduction in supersaturation and consequently a reduction in growth rate. Such a thermodynamic size-dependent effect is usually referred to as the Gibbs–Thomson effect. A continued decrease of NW diameter to a few nanometers eliminates the supersaturation condition in the growing nanoparticle such that NW growth ceases below a minimal critical diameter, d_c, which from Eq. 2.4 is given by

Downloaded by [University of California - San Diego (CDL)] at 19:53 11 December 2013

© 2013 by Taylor & Francis Group, LLC

$$d_c = 4\Omega\alpha_{vs}/\Delta\mu_0. \quad (2.5)$$

Second, NWs grown in different orientations, and therefore with different facets and α_{vs} are expected to result in different d_c. Third, different NW materials have distinguishable $\Omega\alpha_{vs}$ product, and therefore different d_c. Fourth, tuning of $\Delta\mu_0$ with temperature and pressure can change d_c, however at the expense of compromised NW morphology as we shall discuss later. These basic concepts generally apply to all semiconductor NW growth systems.

Since germanium oxide can be easily desorbed from Ge surfaces at $T \geq 300$ °C, which is close to the Ge–Au eutectic temperature and higher than the temperatures at which GeH_4 input precursor decomposes, it is therefore straightforward to conclude that high-quality epitaxial [111] Ge NW growth on Ge(111) surfaces is more readily feasible at ~300 °C than Si. Figure 2.3a shows a plot the temperature profile typically used for the growth of epitaxial [111] Ge NWs on Ge (111) surfaces as demonstrated in Fig. 2.3b. A first high-temperature step is used to desorb germanium oxide and form an eutectic Au–Ge alloy prior to introducing GeH_4 to initiate the Ge NW growth. Once GeH_4 is introduced to the chamber for few tens of seconds, epitaxial growth of the base of the NW is established. The temperature is then quickly reduced to elongate the NW at temperatures that can exclude Ge deposition on the NW sidewalls by vapor–solid growth, and therefore minimize tapering in the NW diameter.

The clean growth procedure of Ge NWs can therefore be used for establishing the size effects in semiconductor NW growth,[35] without the complications of competing reactions in III–V NW growth, or the effects of contaminants or nucleation-deficient conditions in Si NWs that lead to contradictory results.[36] Equation 2.4 predicts that smaller diameter NWs have reduced supersaturations and lower growth rates. This is indeed observed in Ge VLS NW growth as illustrated in Fig. 2.4a, where equally spaced Au metal dots of different sizes have been patterned with electron beam lithography and were subject to Ge NW growth according to the conditions described in Fig. 2.3a. To attain a deeper insight into the governing process at which this drop in growth rate occurs, we consider the variation of the partial pressure or liquidus line with diameter. The diameter-dependent vapor pressure of solute in a Au nanoparticle, $P_{NW}(d)$, can be expressed as a function of its vapor pressure in bulk Au, P_∞, as follows:[25]

Downloaded by [University of California - San Diego (CDL)] at 19:53 11 December 2013

© 2013 by Taylor & Francis Group, LLC

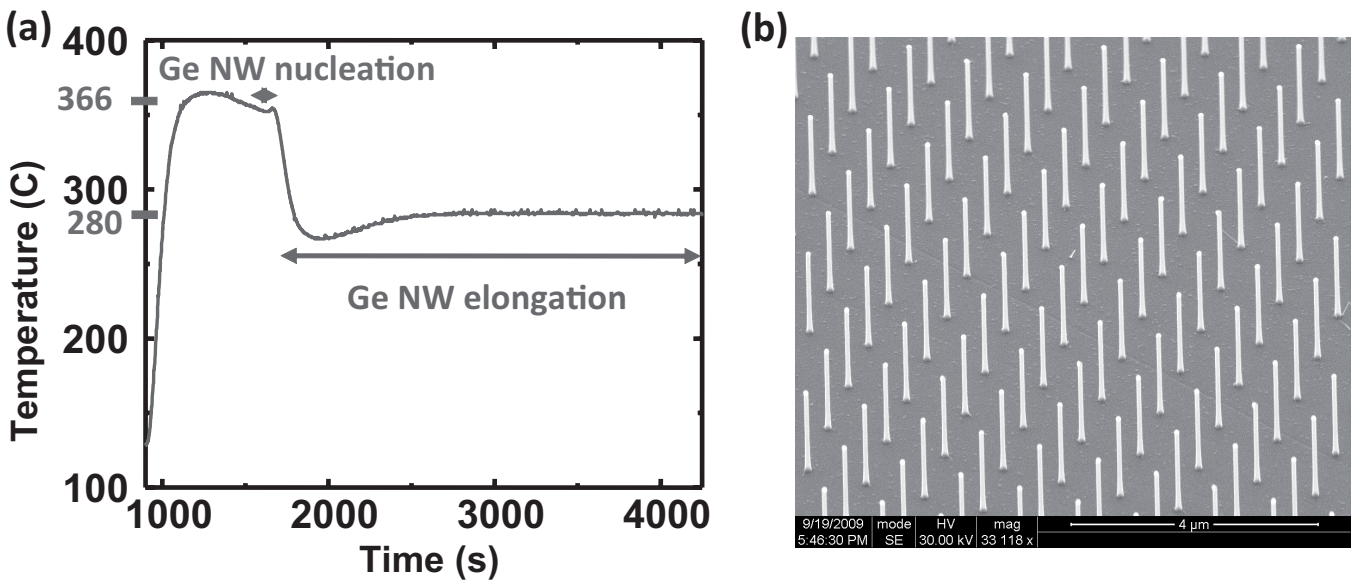

Figure 2.3 (a) Temperature profile for growing epitaxial [111] oriented Ge NWs on a Ge (111) surface as shown in the SEM image of panel (b).

Downloaded by [University of California - San Diego (CDL)] at 19:53 11 December 2013

© 2013 by Taylor & Francis Group, LLC

$$P_{0(\mathrm{NW})}(d) = P_{\infty} exp(4\Omega\alpha_{\mathrm{lv}} / dkT) \cong P_{\infty} exp(4\Omega\alpha_{\mathrm{vs}} / dkT) \qquad (2.6)$$

The term κ is added to Eq. 2.6 to take into account surface energy density changes, and consequently curvature changes of the Au–Ge alloy atop the Ge NW with temperature.[35] We therefore can express the equilibrium Ge concentration in the Au–Ge alloy, $C_{0(\mathrm{NW})}$, as

$$C_{0(\mathrm{NW})} = C_{\infty} \exp(4\kappa\alpha_{\mathrm{vs}} / dkT), \qquad (2.7)$$

which indicates an $exp(1/d)$ increase in the equilibrium concentration of Ge in Au from that of the bulk. Equation 2.7 gives the measured equilibrium concentration of Ge in Au at different temperatures when measured over NWs shown in the array of Fig. 2.4a. It now becomes intuitive to deduce the size-dependent effects in the growth of semiconductor NWs from Fig. 2.4b. Under a constant input partial pressure, that is, constant input Ge concentration at the surface of the Au–Ge eutectic droplet, the concentration gradient with respect to the equilibrium concentration of the Au–Ge eutectic decreases as their diameter decreases, as depicted in Fig. 2.4b. As such, the supersaturation at smaller diameters decreases, and therefore the growth rate decreases at smaller diameters. This can be further deduced from combining Eqs. 2.1 and 2.7 to obtain

$$\Delta\mu / kT = \Delta\mu_0 / kT - (1/\kappa)\ln(C_{0(\mathrm{NW})} / C_{\infty}). \qquad (2.8)$$

Here, at constant growth conditions or supersaturations ($\Delta\mu_0$), a reduction in NW diameter means an increased $C_{0(\mathrm{NW})}$ and therefore a reduced effective supersaturation as deduced from Eq. 2.8 which in turns lead to a reduced growth rate. The dependence of the NW growth velocity (or rate) on supersaturation has been debated extensively, with the generally accepted detailed work of Dubrovskii and Sibirev[37] indicating that such dependence has a dominant quadratic character, validating the original empirical assumptions of Givargizov and Chernov on such dependence.[38] We take the NW growth velocity, $v = dL/dt$, to depend quadratically on the supersaturation in the present case: $v = b(\Delta\mu / kT)^2$, where b is a kinetic coefficient of crystallization that is independent of supersaturation. Thus, Eq. 2.4 can be rearranged as,

$$\sqrt{v} = \sqrt{b}(\Delta\mu_0 / kT) - \sqrt{b}(4\alpha_{\mathrm{vs}} / kT)(1/d). \qquad (2.9)$$

It becomes evident from Eq. 2.9 that in order to examine the dependence of the growth velocity on supersaturation isolated from any other kinetic process, one needs to normalize the growth rate by the kinetic coefficient of crystallization, b, as plotted in Fig. 2.2b.

Downloaded by [University of California - San Diego (CDL)] at 19:53 11 December 2013

© 2013 by Taylor & Francis Group, LLC

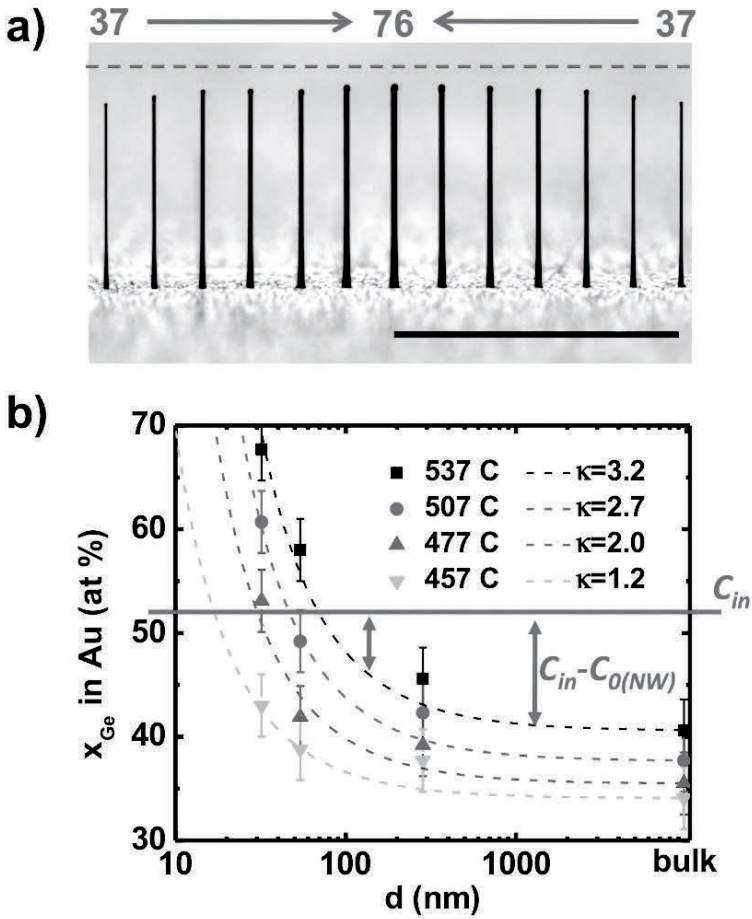

Figure 2.4 (a) SEM image of a linear array of Ge NWs grown from lithographically patterned Au discs. The dashed line highlights the systematic changes in NW length at different diameters. Scale bar is 3 μm. (b) Ge atomic % concentration in Au as a function of diameter at different temperatures. Symbols are experimental data points; dashed lines are fits according to Eq. 2.7. Reprinted with permission from the American Chemical Society, copyright 2010, Ref. [35].

We now discuss the experimental data for Ge VLS NW growth in the context of the size-dependent formalism presented above. Fig. 2.5a shows the NW length as function of diameter for different growth times. Figure 2.5b shows a plot of $v^{1/2}$ as function of $1/d$ for the data

Downloaded by [University of California - San Diego (CDL)] at 19:53 11 December 2013

© 2013 by Taylor & Francis Group, LLC

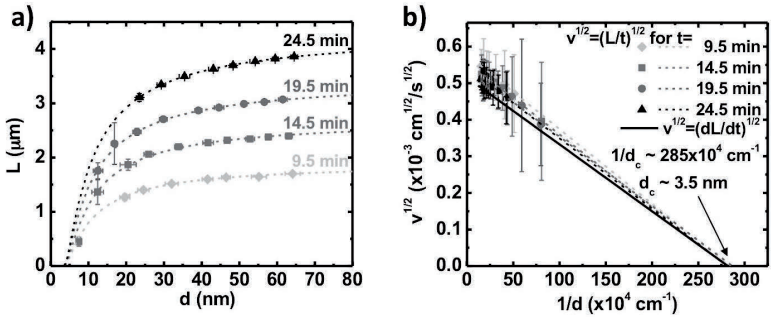

Figure 2.5 (a) Plot of Ge NW length as function of diameter with a P[GeH_4] = 0.6 Torr for different growth times at the low-temperature step [t(276 °C) = 5, 10, 15, and 20 min] resulting in a linear increase of NW length with time for all diameters. (b) Plot of the square root of the growth velocity for the data shown in (a) calculated using $v = L/t$ and using $v = dL/dt$ showing convergence of all data to the same cut-off diameter of ~3.55 nm. Reprinted with permission from the American Chemical Society, copyright 2010, Ref. [35].

of Fig. 2.5a according to the assumption of $v = L/t$ with L and t being the total NW length and growth times, respectively (an assumption that is valid only for long growth times), as well as considering $v = dL/dt$. By fitting the data in Fig. 2.5b with Eq. 2.9, the slope of the fitted lines determines the kinetic coefficient b, and the intercept with the $1/d$ axis determines d_c, from which $\Delta\mu_0$ can be estimated using Eq. 2.5. All fitted lines in Fig. 2.5b lead to a d_c of 3.5 nm, justifying the growth velocity form $v = L/t$ for the present conditions, which becomes valid at sufficiently long growth times. Also integrating Eq. 2.9 is seen to result in an excellent fit to the experimental data of Fig. 2.5a. These experimental results are in agreement with many previous assessments of size-dependent growth rates for Si NWs[39–42] and in contradiction to a few others.[36,43,44] Inconsistencies in size-dependences have been observed when the growth was performed under low SiH_4 or Si_2H_6 partial pressures due to Au loss by diffusion from the Au seed at the NW tips, or due to the presence of oxide masks and contaminants on the growth substrate surface.[36,44] The data presented in Fig. 2.5 clearly shows that a reduction of the growth rate with smaller NW diameters is valid, particularly at optimal growth conditions that lead to controlled NW morphology and orientation such as those NWs shown in Fig. 2.3b. It is worth

Downloaded by [University of California - San Diego (CDL)] at 19:53 11 December 2013

© 2013 by Taylor & Francis Group, LLC

noting that due to their differences in surface energies, atomic volumes, and supersaturations, Si NWs should grow to about 60% smaller diameter than Ge,[41] and changes in growth orientation, that is, in the exposed facets, will influence the minimum diameter.[35]

2.4 Temperature Effects on Nanowire Growth

The most substantial effect on efficient NW nucleation and growth, as well as on the resulting morphology, composition, and doping profiles, arises from temperature effects. For uniform nucleation at the liquid–solid interface and epitaxial NW growth, the growth temperature must be close to or above the eutectic temperature. In some cases, this temperature is sufficiently large for strong decomposition of precursors such as for GeH_4, which leads to concurrent Ge deposition on the NW sidewalls as the NW continues to grow axially. Therefore, the temperature profile for Ge NW growth typically follows that of Fig. 2.3a for successful epitaxial growth with little to no radial coating. The dependence of the growth rate on temperature for VLS NW growth is fairly complex and involves such factors as the relative change of material decomposition, reaction rates at the growth eutectic–NW interface, diffusivity of reactants into, or at the surface of the growth eutectic, diffusion lengths on the substrate and NW sidewalls, etc. Even with the detailed work of Dubrovskii and Sibirev, such complex temperature dependences can lead to incorrect conclusions, particularly when dealing with the temperature dependence of the critical diameter, as we will discuss below.[37]

Experiments typically indicate that a higher growth temperature leads to a more efficient NW nucleation and enhanced growth rates. If that is the case, the question arises as to whether the growth of smaller diameter NWs at higher temperatures becomes more feasible. To answer this question, we must remind the reader that the equilibrium concentration of the semiconductor material in Au increases as the temperature increases. For a constant input precursor partial pressure, this translates to a reduction in the supersaturation as the temperature increases. A reduction in supersaturation causes an increase in d_c according to Eq. 2.5, $d_c = 4\Omega\alpha_{vs}/\Delta\mu_0$, which means that smaller diameter NWs are less likely to grow at higher temperatures. To simplify this argument, let's consider the GeH_4 precursor,

Downloaded by [University of California - San Diego (CDL)] at 19:53 11 December 2013

© 2013 by Taylor & Francis Group, LLC

which is decomposed at the lowest possible growth temperature (~280 °C). Therefore, increasing the temperature above 280 °C does not in principle contribute to extra input Ge concentration at the vapor–liquid interface. It is the increase in the kinetic reaction rates, dictated by the kinetic coefficient b in Eq. 2.9 that leads to an increase in the growth rate with temperature. The supersaturation on the other hand should decrease with temperature. This result can also be deduced from Eq. 2.8 where $C_{0(\mathrm{NW})}$ increases faster with temperature than C_∞. Neglecting this latter dependence of $C_{0(\mathrm{NW})}$ on temperature is what led Dubrovskii and Sibirev to reach a conclusion that the d_c decreases as T increases, which is opposite to the above intuitive argument and what we find in experiments.

The observed temperature dependence of the growth velocity and its impact on the critical size dependence is illustrated in Fig. 2.6a. As $v^{1/2}$ increases with temperature, the intercept with the $1/d$ axis decreases indicating larger d_c, which is plotted as a function of temperature in Fig. 2.8a. To infer the dependence of growth rate on temperature, while excluding other kinetic effects, we plot the growth rate normalized to the kinetic coefficient, v/b, in Fig. 2.6b. A reduced supersaturation with temperature leads to a lower normalized growth rate and larger cut-off diameters as demonstrated in Fig. 2.6b. The detailed dependence of b, $\Delta\mu_0/KT$, and d_c on temperature as extracted from the experimental data of Fig. 2.6 is listed in Table 2.1, which is in excellent agreement with the formalism presented here.

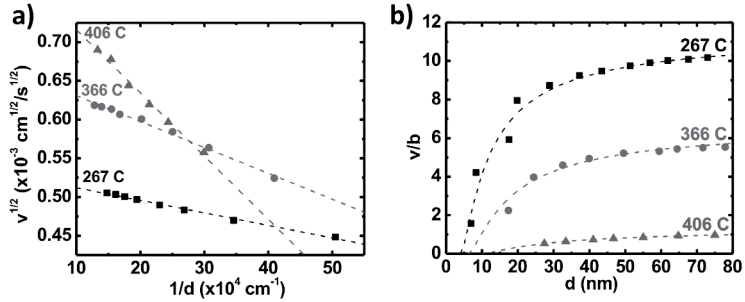

Figure 2.6 (a) Plot of $v^{1/2}$ as a function of $1/d$ at different temperatures of 276 °C, 366 °C, and 406 °C showing different slopes and intercepts. (b) Plot of the growth velocity normalized by the kinetic coefficient b for the data shown in (a). Dashed lines are fits according to Eq. 2.9. Reprinted with permission from the American Chemical Society, copyright 2010, Ref. [35].

Downloaded by [University of California - San Diego (CDL)] at 19:53 11 December 2013

© 2013 by Taylor & Francis Group, LLC

Table 2.1 Calculated kinetic coefficients, supersaturation values, and critical diameters based on measurements for Ge NWs grown at 276 °C, 366 °C, 406 °C, and 440 °C

T (°C)	b (10^{-8} cm/s)	$\Delta\mu_0/kT$	d_c (nm)
276	3.0	3.1	3.4
366	20.5	1.5	6.0
406	80.5	0.9	9.7
440	86.9	0.7	11.6

2.5 Pressure Effects on Nanowire Growth

Similar to temperature, the growth precursor partial pressure effects on NW nucleation, growth, and morphology are substantial. For instance, a straight forward conclusion from Eq. 2.1 indicates that larger supersaturations and growth rates are expected as P_{in} increases. However, as P_{in} increases, some precursors, especially III–V ones, display enhanced decomposition efficiency, an enhanced radial coating, and increased layer stacking in faulty positions during NW growth,[45] with the resulting planar defects typically perpendicular to the growth direction in III–V NWs, and parallel to the growth direction in Si and Ge NWs.[46]

At or near optimal pressure settings for NW growth, the growth behavior is well-described with the formalism presented above. The key features of such dependence can be seen in Fig. 2.7. First, higher P_i leads to higher growth rates, consistent with Eqs. 2.1 and 2.9 where the latter provides the good fit to the data as shown in Fig. 2.7. Second, higher P_i results in lower cut-off diameters as expected from Eq. 2.5, due to an increase in $\Delta\mu_0$. Third, one can see directly from Eq. 2.9 that an increase in P_i will shift $v^{1/2}$ positively (first term dependent on $\Delta\mu_0$) but the slope of $v^{1/2}(1/d)$ remains unchanged (second term in Eq. 2.9), which is also evident in Fig. 2.7b. It is worth noting that a pressure increase also leads to enhanced radial growth, which can compromise the ability to grow smaller NW diameter wires at higher P_i.[35]

We can now summarize the effects of temperature and pressure, and their influence on the critical diameter, d_c, for VLS NW growth as demonstrated in Fig. 2.8. A temperature increase leads to enhanced kinetics and growth velocities, however with a reduced supersaturation that increases the cut-off diameter for growth

Downloaded by [University of California - San Diego (CDL)] at 19:53 11 December 2013

© 2013 by Taylor & Francis Group, LLC

(Fig. 2.8a). A pressure increase causes a larger supersaturation and growth rates and with larger supersaturations, a decrease in d_c is obtained (Fig. 2.8b). These combined effects of temperature and pressure (Figs. 2.6–2.8), as presented here for Ge NW growth, demonstrate clearly key phenomena of the VLS growth mechanism.

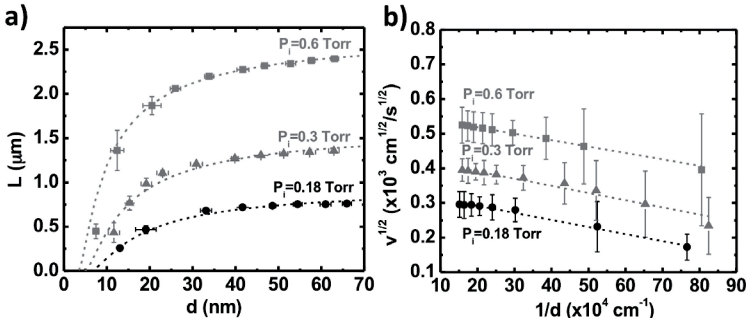

Figure 2.7 (a) Plot of the NW length as a function of diameter for different GeH_4 partial pressures. (b) Plot of $v^{1/2}$ as a function of $1/d$ at different GeH_4 partial pressures for data of (a) showing the progressive reduction in the growth velocity and decrease in critical diameter with increasing pressure. Reprinted with permission from the American Chemical Society, copyright 2010, Ref. [35].

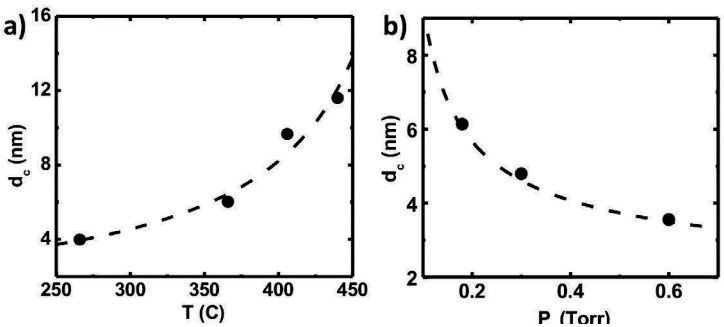

Figure 2.8 (a) Plot of the critical diameter as function of temperature extracted from Fig. 2.6a, illustrating higher cut-off diameters with higher temperatures. The dashed line is calculated according to Eq. 2.5. (b) Plot of the critical diameter as a function of input GeH_4 partial pressure extracted from Fig. 2.7a and showing logarithmic dependence and lower cut-off diameters with higher partial pressures. The dashed line is calculated according to Eq. 2.5, where $\Delta\mu_0$ has been obtained by a fit to the experimental data as function of $\ln|P_i|$.

Downloaded by [University of California - San Diego (CDL)] at 19:53 11 December 2013

© 2013 by Taylor & Francis Group, LLC

2.6 Dopant Precursor Influence on Nanowire Growth

Technological applications of semiconductor NWs require controlled doped interfaces, and the introduction of dopant precursors can have a direct influence on the NW growth rate and morphology. N-type and p-type doping is commonly achieved with the introduction of PH_3 and B_2H_6 reactant gases during NW growth. Fig. 2.9a shows a plot of the pressure normalized growth rate, $v/P_i = L/tP_i$, as a function of $1/d$ for Ge NW growth, which is slightly lowered in the presence of B_2H_6 at small diameters. Introduction of PH_3 into the growth chamber shows that v/P_i is lower than that of undoped NWs for $d \geq 20$ nm (progressively changing from a ~1% reduction at $d = 20$ nm to ~6.5% at $d = 80$ nm), while higher v/P_i are obtained for $d < 20$ nm (again changing from a ~2% increase at $d = 15$ nm to ~22% at $d = 7.5$ nm). Since the normalized supersaturation to partial pressure ratio $\Delta\mu_0/kT/|ln(P_i)|$ is lowered when dopants are introduced (see Table 2.2), this interesting behavior with PH_3 is attributed to a change in surface energy, α_{vs}. Indeed, as one can see in Table 2.2, the $\sqrt{b\alpha_{vs}}$ product remains essentially the same for the cases of GeH_4 and GeH_4/B_2H_6, and lower for the GeH_4/PH_3 case, suggesting a lower α_{vs}, in the latter case after phosphine exposure and resulting in a lower d_c as observed experimentally (Fig. 2.9b and Table 2.2) as deduced from Eq. 2.5. This observation is in general agreement with incorporation of high concentrations of P into the NW sidewalls.[47]

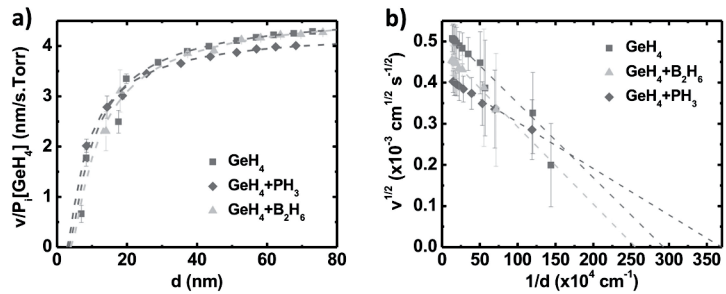

Figure 2.9 (a) Plot of the growth rate normalized by the GeH_4 partial pressure showing a reduction in the growth rate when PH_3 is present during growth. (b) Plot of the square root of the growth rate as a function of inverse diameter illustrating slope and d_c change in the presence of PH_3. Reprinted with permission from the American Chemical Society, copyright 2010, Ref. [35].

Downloaded by [University of California - San Diego (CDL)] at 19:53 11 December 2013

© 2013 by Taylor & Francis Group, LLC

Table 2.2 The calculated critical diameters, pressure-normalized supersaturation values and kinetic coefficients based on measured results for Ge NWs grown with and without dopants at 276 °C using Eqs. 2.5 and 2.9

Precursor	d_c (nm)	$\Delta\mu_0/kT/ln(\lvert P_i\rvert)$	$b^{1/2}\alpha_{vs}$ (10^{-8} J/cm$^{5/2}$/s$^{1/2}$)
GeH_4	3.4	6.0	1.5
GeH_4+B_2H_6	3.9	4.1	1.6
GeH_4+PH_3	2.8	3.7	0.98

Dopant incorporation through the liquid eutectic into the VLS grown semiconductor NW is still a subject of research. Atom probe tomography measurements on Si NWs have shown that the competitive radial deposition from vapor phase growth on the sidewalls of Si NWs (vapor–solid growth) resulted in substantially more efficient dopant incorporation compared with incorporation through the liquid growth eutectic.[47] The degree of doping by such competitive processes depends on the growth conditions, as discussed before. While such processes occur during NW growth, gradients in the doping densities occur in both the radial and axial directions (Fig. 2.10a). Another method for controlled dopant incorporation

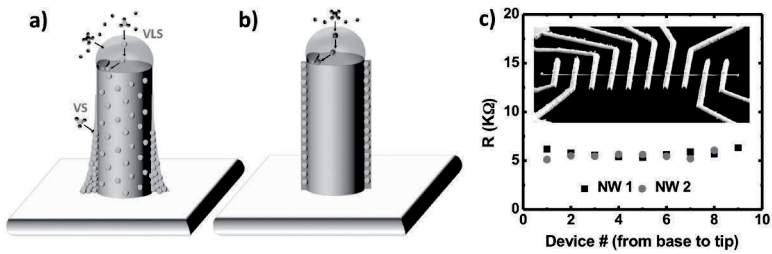

Figure 2.10 (a) Cartoon illustrating competitive incorporation of dopants from the vapor (VS growth) or through the liquid growth eutectic (VLS growth). (b) Doped shells formed on undoped core NWs in a two-step process can result in better axial uniformity of dopants. (c) Plot of the 2-terminal resistance across the entire length (~6 μm) of an i-core/n-shell Ge NW doped using the approach described in (b), showing uniform resistance throughout for two of such devices. Inset is an SEM image of the device labeled NW1.

Downloaded by [University of California - San Diego (CDL)] at 19:53 11 December 2013

© 2013 by Taylor & Francis Group, LLC

in semiconductor NWs is to grow an undoped semiconductor NW and properly alter the growth conditions to prevent axial elongation and induce radial deposition of a conformal doped shell (Fig. 2.10b). Electrical measurements on NWs grown using the latter doping method (i-core/doped-shell) resulted in uniform NW resistance, that is, uniform effective doping, through the entire NW length, as shown in Fig. 2.10c.

2.7 Defects during VLS Growth of Semiconductor Nanowires

Growth according to the VLS mechanism proceeds in a layer-by-layer process with ledge nucleation occurring near the triple-phase interface.[20,48] Because of their small size nucleation and propagation of defects in semiconductor NWs can be dramatically different from that observed in thin film growth, where due to the much larger growth area many defect nucleation sites coexist. At higher supersaturations and growth rates in NWs, the probability of stacking adatoms at faulted locations becomes higher. Wulff constructions have shown that a NW growing in the [111] orientation will have six hexagonal {110} type facets with three inclined {111} planes triangular facets at their intersections (Fig. 2.11). Molecular dynamics (MD) simulations have shown that nucleation occurs at the three triangular facets, $(1\bar{1}1)$ labeled as F_1, $(11\bar{1})$ as F_2, and $(\bar{1}11)$ as F_3, which results in elongation along the NW growth direction in layer-by-layer growth.[49] It is found that in the case of a Si NW, a four-atom cluster on these inclined {111} facets can lead to uniform NW diameter growth. MD simulations have also shown that a dimer formed in a faulted position on F_1, F_2, and F_3 can lead to the nucleation of a SF in the NW. Ledge propagation then occurs from these {111} facets at an inclined angle to the NW growth direction. By considering different possible nucleation sites for each new layer after SF nucleation (Fig. 2.11e), MD simulations have shown that cluster nucleation is energetically favorable by a factor of ~2 (Fig. 2.11f) at the triple-phase interface with the SF. This condition imposes the presence of a single axial defect per NW segment length as we shall see in the experimental results discussed below.

Downloaded by [University of California - San Diego (CDL)] at 19:53 11 December 2013

© 2013 by Taylor & Francis Group, LLC

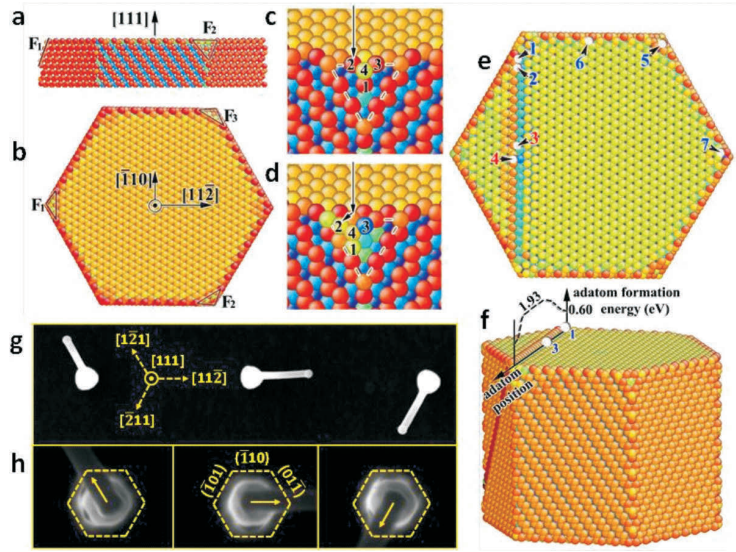

Figure 2.11 (a,b) Side and top view of a [111]-oriented Si NW showing 6 {110} facets with three {111} inclined triangular facets at their intersections where stacking fault (SF) nucleation occurs. (c,d) Side view taken from MD simulations showing nucleation on the (111) F_1 facet in proper (c) or faulted (d) positions. The black arrows are inserted to guide the eye for a four-atom cluster shifting to the faulted position. (e,f) Top (cross-section) and perspective side view of a NW with a SF on the ($1\bar{1}1$) plane as used for MD simulations of nucleation energy barriers at points labeled 1 to 7 in (e). The calculated nucleation energy is superimposed on the structure in (f) and the lowest energy is found at the {110}/SF interface (i.e., SF/triple-phase interface during NW growth). (g,h) High-contrast (g) and low-contrast magnified top view (h) of Ge–Si heterostructure NW grown from lithographically patterned Au dots showing the three possible kink directions (projected onto the top (111) plane) in agreement with MD simulations. Nucleation of the Si segment appears clearly to emerge at two {110} facet interfaces (dashed hexagons in h) corresponding to F_1, F_2, or F_3 in (b). Reprinted with permission from the American Chemical Society, copyright 2011, Ref. [49].

Axial Ge–Si heterostructure NWs provide a natural marker to decisively assess the formation of defects during semiconductor NW growth. Often, an axial Si segment grown on a Ge segment displays a systematic kink from the [111] growth orientation. We utilize this kink to prove that NW nucleation does occur at the {111} facets at

Downloaded by [University of California - San Diego (CDL)] at 19:53 11 December 2013

© 2013 by Taylor & Francis Group, LLC

the interface between two {110} facets. When Ge–Si heterostructure NW growth is performed from lithographically patterned Au dots on (111) Ge surfaces, kinking was typically observed to occur in the three well-defined <112> orientations as projected in the top-view SEM image of Fig. 2.11g. Low-contrast SEM images have revealed that the kink in the Si segment originates at the interface between two {110} facets, as labeled in Fig. 2.11h, consistent with the MD simulation results of nucleation at one of the three {111} facets, labeled F_1, F_2, and F_3 in Fig. 2.11b.

To further resolve defect nucleation in NWs, high-resolution TEM was performed on such axial Ge–Si heterostructures as shown in Fig. 2.12. Detailed analysis of the microstructure of the Si segments, as shown in Fig. 2.12 reveals the presence of a single fault per NW segment that nucleates from the same NW facet (Fig. 2.11b). First, a SF nucleates and propagates in the [112] orientation indicative of a SF on a $(1\bar{1}1)$ growth surface. During layer-by-layer growth, nucleation at the triple-phase interface is pinned at the intersection of the SF with the top liquid–NW interface. As a result, access to the low-energy {111} facet is prohibited, thereby preventing nucleation of any additional faults until the SF is terminated at the opposite side of the NW. This is in complete agreement with the results of Fig. 2.11f and the discussion above. Such a SF requires a NW segment length of $d/\tan(19.5°)$, where d is the NW diameter and 19.5° is the angle between the [112] and [111] orientations, and for the case of Fig. 2.12 is ~85 nm for d = 30 nm, in agreement with experimental observations. Once the SF terminates on the opposite side of the NW, access to the low-energy {111} facet is again permitted as nucleation of the next atomic layer occurs. From Fig. 2.12b, we observe that a twin boundary (TB) is immediately nucleated at the same low-energy $(1\bar{1}1)$ facet at which the preceding SF nucleated, where adatom stacking in two consecutive fault positions leads to TB formation. HRTEM confirms that this process occurs within one atomic bilayer of the termination of the SF with the nucleation switching back to the low-energy $(1\bar{1}1)$ facet. Once formed, the ledge nucleation occurs at the TB/{110} facet interface and propagates on the (111) growth surface (Fig. 2.12b,c). The NW diameter consequently increases just before the kink until the increasing line tension of the stretched liquid Au surface at the triple-phase interface forces the NW growth direction to switch to the [112] orientation, resulting in a 19.5° kink with respect to the initial [111] growth axis. Continuum modeling

Downloaded by [University of California - San Diego (CDL)] at 19:53 11 December 2013

© 2013 by Taylor & Francis Group, LLC

for other cases of NW growth has also noted that perturbations in the line tension of the growth seed may change the NW growth direction.[50] These striking *ex situ* observations of defect nucleation during NW growth establish new features of the VLS mechanism for layer-by-layer NW growth and are supported by the MD simulations discussed earlier.

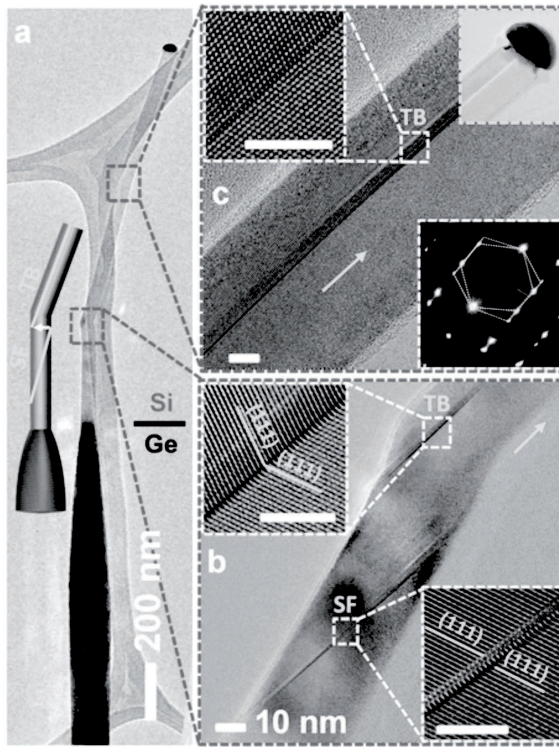

Figure 2.12 (a) TEM image (right side) and cartoon (left side) of a kinked Ge (dark)–Si (bright) axial NW heterostructure. (b) HRTEM image showing nucleation of an intrinsic SF followed by a Σ3 (111) coherent TB from the same NW facet. Both SF and TB nucleate at $(1\bar{1}1)$ facets and propagate along the [112] direction as described in Fig. 2.11. (c) Once formed, the TB pins the nucleation for each new atomic layer at the triple-phase interface and continues to propagate during NW growth allowing no further access to the low-energy (111) facets and thus no additional fault nucleation. The unlabeled scale bars are 5 nm. Arrows in (b) and (c) indicate a [112] NW growth orientation after NW kinking. Reprinted with permission from the American Chemical Society, copyright 2011, Ref. [49].

Downloaded by [University of California - San Diego (CDL)] at 19:53 11 December 2013

© 2013 by Taylor & Francis Group, LLC

With such detailed understanding of defect nucleation in semiconductor NWs on an atomic level, we are now in a position to discuss the more generic behavior of defect nucleation and Au diffusion on semiconductor NWs with "global" pressure and temperature variations. Figure 2.13 shows what we refer to as a *global Si NW growth morphology–structure diagram*. At high temperatures and pressures, Au diffusion and axial twin faults can coexist as shown in Fig. 2.13 (green datum point). If the temperature is kept constant and the pressure is reduced, the growth rate is lowered and fault nucleation is lowered, resulting in single crystal NWs (blue data points in Fig. 2.13). However, Au diffusion is relatively severe under these conditions (black spots in Fig. 2.13 are Au nanoparticles). On the other hand, a high SiH_4 partial pressure but a reduced temperature can result in less Au diffusion but faults and twin boundaries persist due to the high growth rates (black datum point in Fig. 2.13). A low SiH_4 partial pressure and low temperature result in optimal Si NW morphology with single crystal structure and no Au

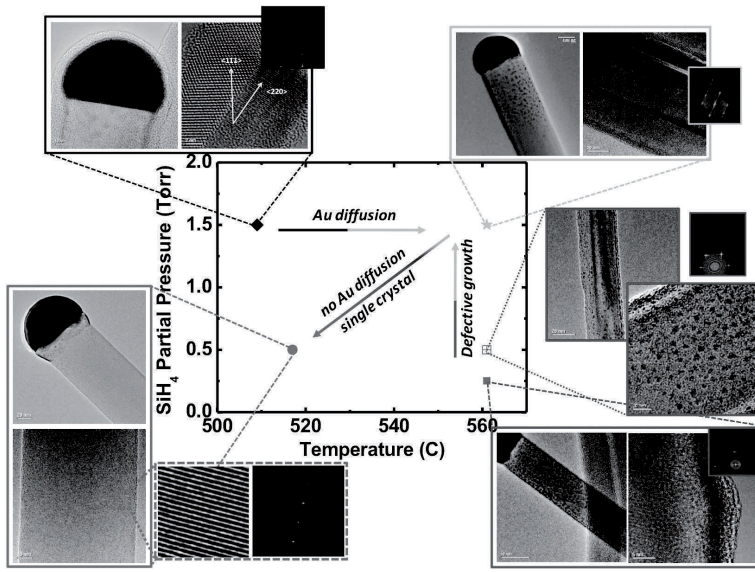

Figure 2.13 *A global Si NW growth morphology–structure diagram* illustrating changes in NW crystal structure, Au diffusion from the growth eutectic droplet, and NW morphology as function of temperature and pressure.

Downloaded by [University of California - San Diego (CDL)] at 19:53 11 December 2013

© 2013 by Taylor & Francis Group, LLC

diffusion. However, at such growth conditions, nucleation efficiency of Si NW growth can dramatically decrease and a compromise has to be dealt with regarding crystal structure and morphology compared with nucleation efficiency.

2.8 Ge Core/Si Shell Heterostructured Nanowires

It has been noted early on that the formation of high-quality epitaxial core/shell materials[51] composed of a semiconducting NW surrounded by one or more single crystal shells can offer opportunities for new control of charge transport in nanostructures.[52] Realizing such heterostructures and assessing their resulting performance is challenging due to the diffusion of the Au growth-mediating seed during Si shell deposition and the typically amorphous nature of the deposited Si shell. The detrimental Au diffusion at higher temperatures, such as for the Ge core/Si shell heterostructures (Fig. 2.14e–h) has been addressed by either introducing O_2 during growth[53] or etching of the Au seed *ex situ* prior to growing Si shells,[54] both of which introduce contaminants that adversely affect the NW properties.

Since Si surface facets have a higher surface energy than Ge,[26] Au diffusion on the Si surface is expected to be less facile than on the Ge surface. Thus, the introduction of a thin Si layer beneath the Au growth seed is anticipated to create a barrier to the Au diffusion down the Ge NW sidewalls. This Au–NW interface energy difference for the Ge and Si NW surface facets should help to stabilize the Au seed at the NW tip to higher temperatures and at lower pressures. Deposition of such an interface layer must be carried out at a low temperature to prevent the onset of Au diffusion along the Ge NW surface prior to formation of the blocking layer. The catalytic effect of the Au nanoparticle was employed to locally decompose SiH_4 to form a thin Si layer below the Au particle at the Ge NW growth temperature (276 °C). When the temperature was ramped to 410 °C, no Au diffusion occurred as depicted in Fig. 2.14i–l, in dramatic contrast to the situation where no Si interfacial barrier layer was grown (Fig. 2.14e–h).

Downloaded by [University of California - San Diego (CDL)] at 19:53 11 December 2013

© 2013 by Taylor & Francis Group, LLC

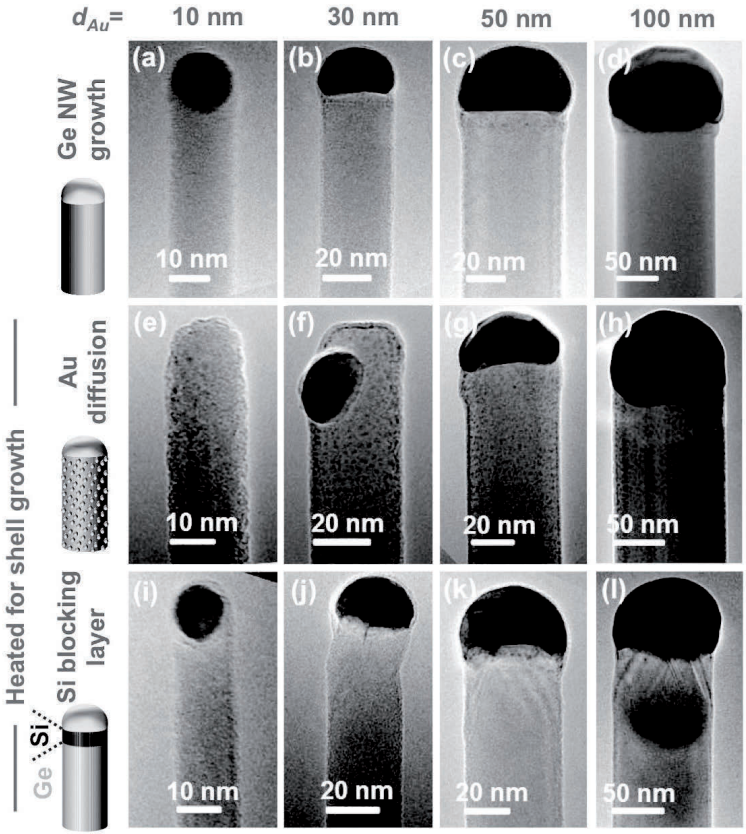

Figure 2.14 TEM images and morphology of different diameter Ge NWs demonstrating inhibition of Au diffusion. (a–d) TEM images of Ge NWs grown at 276 °C from 10 nm, 30 nm, 50 nm, and 100 nm Au nanoparticles, respectively with no Au diffusion. TEM images of Ge NWs grown at 276 °C and subject to a temperature ramp-up to 410 °C; Au diffusion is evident throughout all diameters with total loss of Au nanoparticle for the smallest diameter in (e). (i–l) same as in (e–h), however, with a Si-blocking layer where Au diffusion is blocked and the nanoparticles volume is conserved. Reprinted with permission from the American Institute of Physics, copyright 2011, Ref. [55].

The presence of a Si interfacial layer to block Au diffusion has a dramatic effect on the subsequent growth of Ge and Si shells for heterostructured NWs. Such growth of high-quality shells allows the realization of radial doped structures which can spatially alter

Downloaded by [University of California - San Diego (CDL)] at 19:53 11 December 2013

© 2013 by Taylor & Francis Group, LLC

and confine carriers, leading to improved performance of device structures such as enhanced on-currents or reduced surface scattering in NW field-effect transistors (FETs). Figure 2.15a–c shows a sequence of TEM images of Ge–Si core/shell NWs grown from 10 nm, 30 nm, and 50 nm diameter Au colloids without a Si barrier layer and without maintaining SiH_4 partial pressure during temperature ramp-up, which results in Au diffusion and a rough Si shell morphology. With a low-temperature Si interfacial barrier layer and a SiH_4 partial pressure of 125 mTorr during temperature ramp up, Au diffusion on the Ge NW sidewalls was avoided and single crystal Ge–Si core/shell NWs were grown in a single growth run as demonstrated in Fig. 2.15d–f. The Si shell thickness was chosen to be ~3 nm, which is within the coherent critical thickness limit for all Ge core diameters and hence ensures high crystalline quality of the Si shells without misfit dislocations.

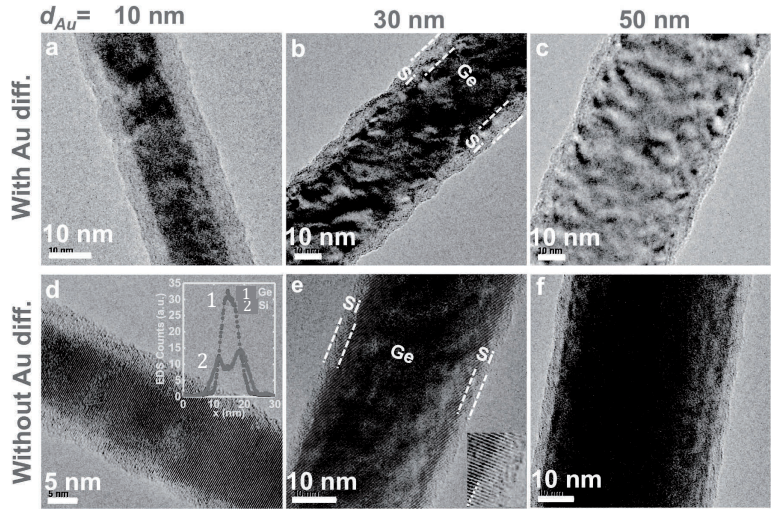

Figure 2.15 (a–c) TEM images of Ge–Si core/shell NWs grown at 276/500 °C from 10 nm, 30 nm, and 50 nm Au colloids, respectively, *without* a low-temperature Si barrier layer leading to 5–7 nm thick Si shells and rough NW surface morphologies. (d–f), TEM images of Ge–Si core/shell NWs grown at 276/500 °C from 10 nm, 30 nm, and 50 nm Au colloids, respectively, with a low-temperature Si barrier layer and a SiH_4 partial pressure of 0.25 Torr during temperature ramp (10 min) and Si shell deposition (7 min) leading to a 3 nm thick single crystal Si shell. Reprinted with permission from the American Institute of Physics, copyright 2011, Ref. [56].

Downloaded by [University of California - San Diego (CDL)] at 19:53 11 December 2013

© 2013 by Taylor & Francis Group, LLC

The new understanding of the interplay between interface energies and Au diffusion on NW sidewalls for morphology control over Ge–Si core/shell heterostructures enable a single step growth process for high-quality growth of single crystal heterostructures. This provides a route for such synthesis without having to expose the NWs to *ex situ* chemical treatments that adversely affect their morphology,[54] or to *ex situ* thermal treatments that may induce thermally driven contaminants into the Si shell and Ge core and diffuse their otherwise abrupt interface.[51] With such a growth approach, a 2× improvement in experimental hole mobility, transconductance, and on-currents was demonstrated for heterostructures with smooth surface morphologies compared with those with rough surface morphologies and record on-currents for p-type FET devices were achieved.[55,56]

2.9 Unique Opportunities for Bandgap Engineering in Semiconductor Nanowires

The most compelling aspect of the VLS growth approach is the potential to modulate doping and composition along the length of the NW during its layer-by-layer growth,[57,58] thereby enabling energy band-edge engineering along the NW axis for additional control over charge transport. This control is in contrast to planar device growth where composition modulation in the charge transport direction (in-plane) is typically not possible during material growth which proceeds in the orthogonal (out-of-plane) direction.[59] This aspect is particularly attractive for heterostructured tunneling FET devices to simultaneously achieve steep turn on transistor characteristics while dramatically reducing the leakage current in the off state.[60,61]

Ge–Si heterostructured NWs not only offer two different charge injection and collection barriers at the metal semiconductor interfaces, but also add the important ability to accommodate band-offsets and built-in electric fields in the conduction or valence bands, separately at the Ge and Si sides of the NW, by proper selection of metal–semiconductor barrier heights with the metal contacts. The axial compositional asymmetry and band-offset accommodation, if chosen properly, can assist in more efficient sweeping of injected carriers from one terminal to the other and minimize or eliminate carrier leakage in the opposite direction. For the device demonstrated in Fig. 2.16,[62] a p+ doped Ge NW shell on i-Ge core, followed by an

Downloaded by [University of California - San Diego (CDL)] at 19:53 11 December 2013

© 2013 by Taylor & Francis Group, LLC

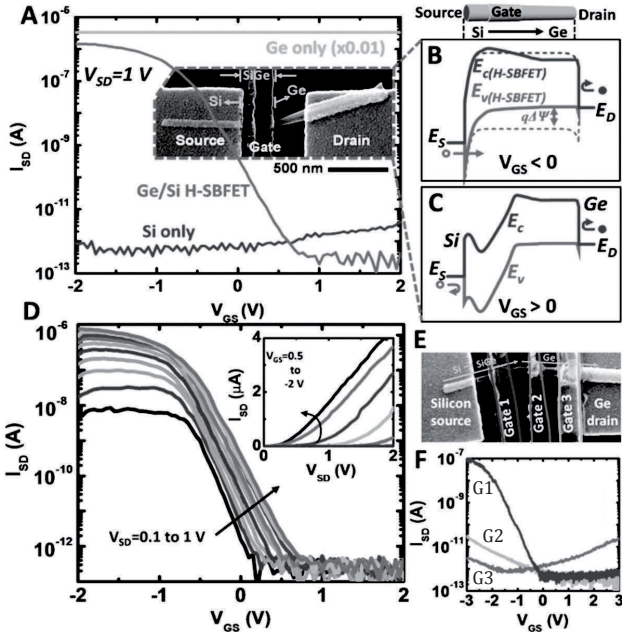

Figure 2.16 (a) Transfer curves of a p⁺Ge–Si NW heterostructure S-TFET showing 10^7 I_{on}/I_{off} ratio. Devices fabricated in the same process on reference p⁺Ge segments showed no gate modulation and those on reference Si segments showed ambipolar behavior over a larger V_{GS} range. (b,c) Simulated energy band-edge diagrams, extracted from the center of the NW channel, illustrating device operation where V_D is applied to the Si side (left, labeled as source) using the same gate configuration as in (a). A pure Si channel [dashed band-edge diagram in (b)] lifts up the potential by $\Delta\Psi$ in the channel therefore reducing the probability of hole emission into the channel and eliminating the built-in field in the valence band, only attained with the heterostructure. (d) Transfer curves at several V_{DS} biases showing no source-drain leakage and no ambipolar transport. Threshold-voltage shifts toward positive voltage are due to the lowering of the Schottky-barrier height at higher V_{DS} biases. Inset shows output characteristics of the same device. (e) SEM image of a multiple-gate device on a single Ge–Si axial NW heterostructure. (f) Transfer curves with V_D applied to the Si side of the device and gate voltage applied to gate 1 (G1), gate 2 (G2), and gate 3 (G3). Current modulation as function of V_{GS} is strongest near the Si side of the device (G1) and is weakest on the Ge side of the device (G1 and G2). Reprinted with permission from the American Institute of Physics, copyright 2011, Ref. [62].

Downloaded by [University of California - San Diego (CDL)] at 19:53 11 December 2013

© 2013 by Taylor & Francis Group, LLC

undoped axial Si segment was grown and heterostructure Schottky barrier FETs (H-SBFETs) were fabricated. As shown in Fig. 2.16a, the highly doped Ge NWs show high currents with no current modulation over a large gate bias range, indicating no channel and no barrier modulation for the Ge segments. Low currents and no gate bias dependence were also observed for Si NWs within the gate voltage range shown in Fig. 2.16a. In contrast, a Si–Ge heterostructure NW shows seven orders of magnitude current modulation for the same source-drain bias voltage (V_{SD} = 1 V) as shown in Fig. 2.16a.

The high on-current observed in the axial Ge–Si heterostructure compared with that of homogeneous Si devices results from accommodation of the Ge to Si band offset being mostly in the valence band at the Si side of the channel, which provides an additional field that can assist hole thermoionic emission at the Si source (see band diagrams in Fig. 2.16b,c). This interpretation of transport behavior is also supported with another device with multiple gates placed along the channel of the Ge–Si axial NW heterostructure where transconductance is maximal for the gate placed on the Si segment of the device near the Ni source contact (Fig. 2.16e,f). This enhanced combined performance of high on-currents, high I_{on}/I_{off} ratios, and elimination of ambipolar behavior for this heterostructured S-TFET has not been reported in previous TFET devices. Such an axial band-edge-engineered device is made possible through the composition modulation achieved during the VLS growth process.

2.10 Conclusions

In this chapter we review and provide new perspectives on the VLS growth mechanism in semiconductor NWs along with detailed experimental evidence of emergent size effects in the growth and heterostructuring of Ge/Si NWs. Our analysis of size effects in the synthesis of Ge NWs provides the first direct and quantitative validation of a thermodynamic limit on the achievable NW diameter in VLS growth by combining observations of the reduced growth rate and enhanced equilibrium Ge solubility in the liquid Au–Ge growth seeds. The unified framework for understanding these nanoscale size effects—based on the Gibbs–Thomson effect—provides a basis for analyzing the cutoff diameter and other size-dependent growth phenomena at small diameters for a wide variety

Downloaded by [University of California - San Diego (CDL)] at 19:53 11 December 2013

© 2013 by Taylor & Francis Group, LLC

of semiconductor materials that form NWs by the VLS process. Aside from conventional growth parameters, such as temperature and precursor pressure, surface energies are a key factor in synthesis processes at the nanoscale, as demonstrated in the section on the influence of dopants. By tracking defect nucleation and propagation as a fingerprint of the layer-by-layer growth process in heterostructured NWs, a more complete understanding of the VLS growth mechanism, fault nucleation and NW kinking is enabled. We have also highlighted the influence of surface energies on controlling NW morphology, particularly for the case of Ge/Si core/shell NWs where we demonstrate how this effect can be used to block Au sidewall diffusion to produce optimal heterostructured NWs in a single growth step. These combined processes provide an improved and unified understanding of the VLS growth mechanism. We also demonstrate how to utilize these methods to achieve devices uniquely grown by the VLS method for Ge–Si axial heterostructures that provide enhanced performance compared with their homogenous counterparts. Such key concepts in NW growth and devices are envisioned to bring maturity to the field of semiconductor NWs and the technological applications they promise.

Acknowledgments

This research was funded in part by the Laboratory Directed Research and Development Program at Los Alamos National Laboratory and performed, in part, at the Center for Integrated Nanotechnologies, a U.S. Department of Energy, Office of Basic Energy Sciences user facility at Los Alamos National Laboratory (Contract DE-AC52-06NA25396).

References

1 G. W. Sears, A Growth Mechanism for Mercury Whiskers. *Acta Metal.* **3**, 361 (1953).

2 E. S. Greiner, J. A. Gutowski, and W. C. Ellis. Preparation of Silicon Ribbons. *J. Appl. Phys.* **32**, 2489 (1961).

3 R. S. Wagner, and W. C. Ellis, Vapor-Liquid-Solid Mechanism of Single Crystal Growth. *Appl. Phys. Lett.* **4**, 89 (1964).

4 K. Haraguchi, T. Katsyama, K. Hiruma, and K. Ogawa. GaAs p-n Junction Formed in Quantum Wire Crystals. *Appl. Phys. Lett.* **60**, 745 (1992).

Downloaded by [University of California - San Diego (CDL)] at 19:53 11 December 2013

© 2013 by Taylor & Francis Group, LLC

5 A. M. Morales, and C. M. Lieber. A Laser Ablation Method for the Synthesis of Crystalline Semiconductor Nanowires. *Science* **279**, 208 (1998).

6 J. Johansson *et al.* Structural Properties of <111>B-oriented III–V Nanowires. *Nature Materials* **5**, 574 (2006).

7 R. Rosario *et al.* Lotus Effect Amplifies Light-Induced Contact Angle Switching. *J. Phys. Chem. B* **108**, 12640 (2004).

8 C. Thelander *et al.* Electron Transport in InAs Nanowires and Heterostructure Nanowire Devices. *Solid State Commun.* **131**, 573 (2004).

9 J. C. Johnson, H. Yan, P. Yang, and R. J. Saykally. Optical Cavity Effects in ZnO Nanowire Lasers and Waveguides. *J. Phys. Chem. B* **107**, 8816 (2003).

10 P. Martin, Z. Aksamija, E. Pop, and U. Ravaioli. Impact of Phonon-Surface Roughness Scattering on Thermal Conductivity of Thin Si Nanowires. *Phys. Rev. Lett.* **102**, 125503 (2009).

11 J. Y. Huang *et al.* In Situ Observation of the Electrochemical Lithiation of a Single SnO_2 Nanowire Electrode. *Science* **330**, 1515 (2010).

12 C. Thelander *et al.* Nanowire-based One-dimensional Electronics. *Mater. Today* **9**, 28 (2006).

13 P. J. Pauzauskie, and P. Yang. Nanowire Photonics. *Mater. Today* **9**, 36 (2006).

14 A. I. Boukai *et al.* Silicon Nanowires as Efficient Thermoelectric Materials. *Nature* **451**, 168 (2008).

15 C. K. Chan *et al.* High Performance Lithium-Battery Anodes Using Silicon Nanowires. *Nature Nano.* **3**, 31 (2008).

16 V. Schmidt, J. V. Wittemann, S. Senz, and U. Gosele. Silicon Nanowires: A Review on Aspects of their Growth and their Electrical Properties. *Adv. Mat.* **21**, 2681 (2009).

17 S. A. Dayeh. Electron Transport in Indium Arsenide Nanowires. *Semicond. Sci. Technol.* **25**, 024004 (2010).

18 S. T. Picraux, S. A. Dayeh, P. Manandhar, D. E. Perea, and S. G. Choi. Silicon and Germanium Nanowires: Growth, Properties, and Integration. *JOM*. **62**, 35 (2010).

19 H. Wang, and G. S. Fischman. Role of Liquid Droplet Surface Diffusion in the Vapor-Liquid-Solid Whisker Growth Mechanism. *J. Appl. Phys.***76**, 1557 (1994).

Downloaded by [University of California - San Diego (CDL)] at 19:53 11 December 2013

© 2013 by Taylor & Francis Group, LLC

20 F. Glas, J.-C. Harmand, and G. Patriarche. Why Does Wurtzite Form in Nanowires of III-V Zinc Blende Semiconductors. *Phys. Rev. Lett.* **99**, 146101 (2007).

21 C.-Y. Wen *et al.* Formation of Compositionally Abrupt Axial Heterojunctions in Silicon-Germanium Nanowires. *Science* **27,** 1247 (2009).

22 A. D. Gamalski, J. Tersoff, R. Sharmas, C. Ducati, and S. Hofmann. Formation of Metastable Liquid Catalyst During Subeutectic Growth of Germanium Nanowires. *Nano Lett.* **10**, 2972 (2010).

23 V. N. Smirnov, Germane Decomposition: Kinetic and Thermochemical Data. *Kinet. Catal.* **48**, 1608 (2007).

24 B. S. Meyerson, and J. M. Jasinski, Silane Pyrolysis Rates for the Modeling of Chemical Vapor Deposition. *J. App. Phys.* **61**, 785 (1987).

25 L. E. Fröberg, W. Seifert, and J. Johansson. Diameter Dependent Growth Rate of InAs Nanowires. *Phys. Rev. B* **76**, 153401 (2007).

26 Q. Jiang, H. M. Lu, and M. Zhao. Modeling of Surface Energies of Elemental Crystals. *J. Phys.: Condens. Matter.* **16**, 521 (2004).

27 T. Y. Tan, N. Li, and U. Gosele. Is There a Thermodynamic Size Limit of Nanowires Grown by the Vapor-Liquid-Solid Process. *Appl. Phys. Lett.*, **183**, 1199 (2007).

28 C.-Y. Wen, M. C. Reuter, J. Bruley, J. Tersoff, S. Kodambaka, E. A. Stach, F. M. Ross, Formation of Compositionally Abrupt Axial Heterojunctions in Silicon-Germanium Nanowires. *Science* **326**, 1247 (2009).

29 S. Kodambaka, J. Tersoff, M. C. Reuter, and F. M. Ross. Germanium Nanowire Growth below the Eutectic Temperature. *Science* **316**, 729 (2007).

30 S. A. Dayeh, E. T. Yu, and D. Wang. III-V Nanowire Growth Mechanism: V/III Ratio and Temperature Effects. *Nano Lett.* **7**, 2486 (2007).

31 S. A. Dayeh, E. T. Yu, and D. Wang. Surface Diffusion and Substrate-Nanowire Adatom Exchange in InAs Nanowire Growth. *Nano Lett.* **9**, 1967 (2009).

32 P. Aella, S. Ingole, W. T. Petuskey, and S. T. Picraux. Influence of Plasma Stimulation on Si Nanowire Nucleation and Orientation Dependence. *Adv. Mat.* **19**, 2603 (2007).

33 S. A. Dayeh, C. Soci, X. Bao, and D. Wang. Advances in the Synthesis of InAs and GaAs Nanowires for Electronic Applications. *Nano Today* **4**, 347 (2009).

Downloaded by [University of California - San Diego (CDL)] at 19:53 11 December 2013

© 2013 by Taylor & Francis Group, LLC

34 K. A. Dick *et al.* A New Understanding of Au-assisted Growth of III-V Nanowires. *Adv. Func. Mat.* **15**, 1603 (2005).

35 S. A. Dayeh, and S. T. Picraux. Direct Observation of Nanoscale Size Effects in Ge Semiconductor Nanowire Growth. *Nano Lett.***10**, 4032 (2010).

36 H. Schmid, M. T. Bjork, J. Knoch, H. Riel, and W. Riess. Patterned Epitaxial Vapor-Liquid-Solid Growth of Silicon Nanowires on Si(111) Using Silane. *J. App. Phys.* **103**, 024304 (2008).

37 Dubrovskii, V. G., and Sibirev N. V. Growth Rate of a Crystal Facet of arbitrary Size and Growth Kinetics of Vertical Nanowires. *Phys. Rev. E* **70**, 031604 (2004).

38 Givargizov, E. I., and Chernov A. A. Rate of Whisker Growth by the Vapor-Liquid-Crystal Mechanism and the Role of Surface Energy. *Kristalografiya* **18**, 147 (1973).

39 Givargizov, E. I. Fundamental Aspects of VLS Growth. *J. Cryst. Growth* **31**, 20 (1975).

40 Wu, Y., Fan, R., Yang, P. Block-by-Block Growth of Single-Crystalline Si/SiGe Superlattice Nanowires. *Nano Lett.* **2**, 83 (2002).

41 X. Zhang, K.-K. Lew, P. Nimatoori, J. M. Redwing, and E. C. Dickey. Diameter-Dependent Composition of Vapor-Liquid-Solid Grown $Si_{1-x}Ge_x$ Nanowires. *Nano Lett.* **7**, 3241 (2007).

42 T. E. Clark, P. Nimmatoori, K.-K. Lew, L. Pan, J. M. Redwing and E. C. Dickey, E. C. Diameter Dependent Growth Rate and Interfacial Abruptness in Vapor-Liquid-Solid $Si/Si_{1-x}/Ge_x$ Heterostructure Nanowires. *Nano Lett.* **8**, 1246 (2008).

43 J. Weyher. Some Notes on the Growth Kinetics and Morphology of VLS Silicon Crystals Grown with Platinum and Gold as Liquid-Forming Agents. *J. Cryst. Growth* **43**, 235 (1978).

44 S. Kodambaka, J. Tersoff, M. C. Reuter, and F. M. Ross. Diameter-Independent Kinetics in the Vapor-Liquid-Solid Growth of Si Nanowires. *Phys. Rev. Lett.* **96**, 096105 (2006).

45 R. E. Algra *et al.* Twinning Superlattices in Indium Phosphide Nanowires. *Nature* **456**, 369 (2008).

46 F. M. Davidson, D. C. Lee, D. D. Fanfair, and B. A. Korgel. Lamellar Twinning in Semiconductor Nanowires. *J. Phys. Chem. C* **111**, 2929 (2007).

Downloaded by [University of California - San Diego (CDL)] at 19:53 11 December 2013

© 2013 by Taylor & Francis Group, LLC

47 D. E. Perea *et al.* Direct Measurement of Dopant Distribution in an Individual Vapor-Liquid-Solid Nanowire. *Nat. Nanotechnol.* **4**, 315 (2009).

48 S. H. Oh, M. F. Chisholm, Y. Kauffmann, W. D. Kaplan, W. Luo, M. Rühle, and C. Scheu. Oscillatory Mass Transport in Vapor-Liquid-Solid Growth of Sapphire Nanowires. *Science* **330**, 489 (2010).

49 S. A. Dayeh, J. Wang, N. Li, J. Y. Huang, A. V. Gin, and S. T. Picraux. Growth, Defect Formation and Morphology Control of Germanium-Silicon Semiconductor Nanowire Heterostructures, *Nano Letters* **11**, 4200, (2011).

50 K. W. Schwarz, and J. Tersoff. From Droplets to Nanowires: Dynamics of Vapor-Liquid-Solid Growth. *Phys. Rev. Lett.* **102**, 206101 (2009).

51 L. J. Lauhon, M. S. Gudiksen, D. Wang, and C. M. Lieber. Epitaxial Core-shell and Core-multishell Nanowire Heterostructures. *Nature* **420**, 57 (2002).

52 G. Liang, J. Xiang, N. Kharche, G. Klimeck, C. M. Lieber, and M. Lundstrom. Performance Analysis of a Ge/Si Core/Shell Nanowire Field Effect Transistor. *Nano Lett.* **7**, 642 (2007).

53 S. Kodambaka, J. B. Hannon, R. M. Tromp, and F. M. Ross. Control of Si Nanowire Growth by Oxygen. *Nano Lett.* **6**, 1292 (2006).

54 I. A. Goldthrope, A. F. Marshall, and P. C. McIntyre. Inhibiting Strain-Induced Surface Roughening: Dislocation-Free Ge/Si and Ge/SiGe Core—Shell Nanowires. *Nano Lett.* **9**, 3715 (2009).

55 S. A. Dayeh, N. H. Mack, J. Y. Huang, and S. T. Picraux. Advanced Core/Multi-shell Germanium/Silicon Nanowire Heterostructures: The Au Diffusion Bottleneck. *Appl. Phys. Lett.* **99**, 023102 (2011).

56 S. A. Dayeh, A. V. Gin, and S. T. Picraux. Advanced Core/Multi-shell Germanium/Silicon Nanowire Heterostructures: Transport and Morphology. *Appl. Phys. Lett.* **98**, 163112 (2011).

57 M. S. Gudiksen, L. J. Lauhon, J. Wang, D. C. Smith, and C. M. Lieber. Growth of Nanowire Superlattice Structures for Nanoscale Photonics and Electronics. *Nature* **415**, 617 (2002).

58 M. T. Bjork *et al.* One-dimensional Steeplechase for Electrons Realized. *Nano Lett.* **2**, 87 (2002).

59 M. L. Lee, E. A. Fitzgerald, M. T. Bulsara, M. T. Currie, and A. Lochtefeld. Strained Si, SiGe, and Ge Channels for High-Mobility Metal-Oxide-

Downloaded by [University of California - San Diego (CDL)] at 19:53 11 December 2013

© 2013 by Taylor & Francis Group, LLC

Semiconductor Field-Effect Transistors. *J. Appl. Phys.* **97**, 011101 (2005).

60 O. M. Nayfeh *et al.* Design of Tunneling Field-Effect Transistors using Strained-Silicon/Strained-Ge Type-II Staggered Heterojunctions. *IEEE Elect. Dev. Lett.* **29**, 1074 (2008).

61 L. Wang, E. Yu, Y. Taur, and P. Asbeck. Design of Tunneling Field-Effect Transistors Based on Staggered Heterojunctions for Ultralow-Power Applications. *IEEE Elect. Dev. Lett.* **31**, 431 (2010).

62. S. A. Dayeh, R. M. Dickerson, and S. Tom Picraux. Axial Bandgap Engineering in Germanium-Silicon Heterostructured Nanowires. *Appl. Phys. Lett.* **99**, 113105 (2011).

Downloaded by [University of California - San Diego (CDL)] at 19:53 11 December 2013

© 2013 by Taylor & Francis Group, LLC